

In pursuit of damage tolerance in engineering and biological materials

Robert O. Ritchie

This article is based on a presentation given by Robert O. Ritchie for the David Turnbull Lectureship on December 3, 2013, at the Materials Research Society Fall Meeting in Boston. Ritchie received this award for his “pioneering contributions to, and teaching us all how to think about, the mechanistic role of microstructure in governing fatigue and fracture in a variety of materials systems, and communicating his scientific insights to the world audience through eloquent lectures and seminal publications.”

The ability to image and quantify material behavior in real time at nano to near-macro length scales, preferably in three dimensions, is a crucial feature of modern materials science. Here, we examine such an approach to characterize the mechanical properties of three diverse classes of materials: (1) biological materials, principally bone, using both *in situ* small-/wide-angle x-ray scattering/diffraction to probe nanoscale deformation behavior and x-ray computed microtomography to study microscale damage mechanisms; (2) biomimetic materials, specifically a nacre-like ceramic, where microtomography is used to identify toughening mechanisms; (3) synthetic materials, specifically ceramic textile composites, using *in situ* microtomography to quantify the salient mechanical damage at ultrahigh temperatures. The mechanistic insights for the understanding of damage evolution and fracture afforded by these techniques are undeniable; as such, they can help provide a basis for the achievement of enhanced damage tolerance in structural materials.

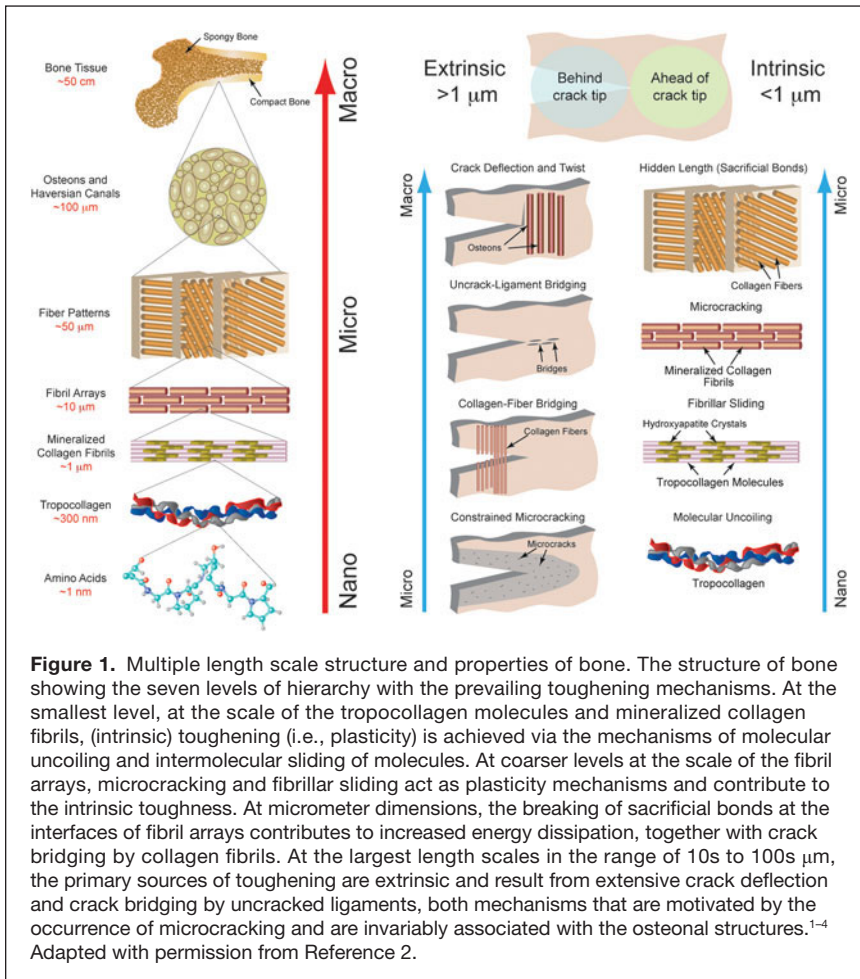
Introduction

One of the hallmarks of modern materials science is the attempt to understand material behavior over a range of length scales, from nanoscale to macroscopic dimensions. This “mesoscale” (or multiscale) perspective is imperative, as materials, especially biological and natural materials, have characteristic structural features that span most of these length scales; moreover, it is at these differing scales where their specific properties originate. An excellent case in point is human bone, which like most biological materials has a complex hierarchical structure spanning from atomic dimensions, where the twisting of peptide chains form collagen molecules, to the osteonal structures at near-millimeter dimensions (i.e., the roughly cylindrical structures in cortical bone through which bone remodels) (**Figure 1**).^{1,2}

Distinguishing these scales is critical, as the mechanisms that contribute to strength and ductility in bone, specifically those associated with the generation of plasticity, are created largely at submicrometer dimensions, similar to the nanoscale dimensions of the Burger’s vectors that control dislocation plasticity in metals. Toughness for bone, however, is *additionally* generated at much coarser dimensions—at the tens to hundreds of microns—as the crack path interacts with the bone-matrix

structure. These crack/microstructure interactions primarily involve large structural features such as osteons, which serve to generate crack deflection and bridging mechanisms that “shield” the crack from the applied driving force (i.e., they lessen the local stresses and strains experienced by the crack).³ Indeed, the union of these mechanisms represents the essence of fracture resistance in materials: respectively, intrinsic toughening arising from resistance to damage *ahead* of the tip of a crack, motivated by plasticity mechanisms generated at the nanoscale, paired with extrinsic toughening associated with crack-tip shielding mechanisms generated at the microscale largely *behind* the crack tip (Figure 1).⁴

To explore the relevance of these multiple-scale concepts to the overall mechanical behavior of materials, we need to characterize both structure and mechanical properties at many differing dimensions. Here, we describe the use of several such techniques involving macroscale fracture mechanics, microscale *in situ* x-ray computed microtomography (μ -CT) and scanning electron microscopy, and nanoscale *in situ* small-/wide-angle x-ray scattering/diffraction (SAXS/WAXD) to examine the sources of structural damage and fracture resistance in several divergent classes of materials, specifically



biological materials such as bone, mollusk shells and their man-made biomimetic counterparts, and ultrahigh-temperature ceramic-matrix composites (CMCs) designed for gas-turbine and hypersonic applications.

Techniques

To characterize the deformation and fracture properties of materials over a range of length scales, we utilized several experimental techniques. At the macroscale, we use standard uniaxial tensile/bend testing and fracture mechanics methodologies. However, to add real-time imaging and quantification of material behavior at smaller length scales, these routine tests can be performed *in situ* in the x-ray synchrotron and in the environmental scanning electron microscope (eSEM). With respect to the former, the application of two specific procedures are described here where *in situ* tensile testing is carried out (1) on samples of bone with simultaneous SAXS/WAXD analysis to partition the strain between the collagen and mineral,⁵ and (2) on biomimetic ceramics and ceramic-matrix composites, with simultaneous μ -CT to image and quantify the crack paths and damage mechanisms at temperatures up to 1850°C.⁶ We also show how *in situ* fracture-toughness testing inside the eSEM to determine crack-resistance curves

(R-curves)* can provide crucial information on crack-path interactions with relevant microstructural features that form the basis of extrinsic toughening.

SAXS/WAXD

Strength and ductility measurements are made using uniaxial tension tests under conditions where simultaneous SAXS/WAXD patterns can be obtained in real time. For bone, this enables estimation of the individual strains in the collagen and mineral phases at any given strain on the whole tissue. As shown in **Figure 2**, hydrated samples are mounted in a load frame in the synchrotron facility with the long axis oriented perpendicular to a parallel beam of monochromatic 10 keV x-rays.⁷ During loading, SAXS/WAXD measurements are taken at various points along the stress/strain curves; radiation doses are maintained below 30 kGy to minimize tissue damage. In the case of the SAXS measurements, it should be noted that the meridional collagen molecules in the fibril have a staggered spacing of ~ 67 nm (where the mineral is deposited between the heads and tails of the collagen), leading to a diffraction pattern. In the case of the WAXD measurements, the detector is placed much closer to the sample and oriented to get diffraction of the (0002) peak (which is parallel to the long axis of the collagen molecules) at a mineral

lattice spacing of ~ 0.344 nm. Details on this technique are given elsewhere.^{5,7}

X-ray computed microtomography

For synchrotron computed microtomography of bone, we use 18 keV incident x-ray energy with a 350 ms exposure time, giving a spatial resolution between 0.65–1.8 μm per voxel. *In situ* tomography cannot be reliably performed on bone, as irradiation exposure typically is ~ 1 MGy, which damages the tissue;⁸ accordingly, we use tomography to characterize bone-mineral density and osteonal spacings, and to assess damage and crack paths *ex situ*. *In situ* μ -CT during tensile testing, however, can be performed on synthetic materials

*The R-curve provides an assessment of the fracture toughness in the presence of subcritical crack growth involving measurements of the crack-driving force (e.g., the stress intensity K or J -integral) (i.e., the rate of change in potential energy per unit increase in crack area) as a function of crack extension (Δa). The value of the driving force at $\Delta a \rightarrow 0$ provides a measure of the crack-initiation toughness, whereas the slope of the R-curve can be used to characterize the crack-growth toughness.

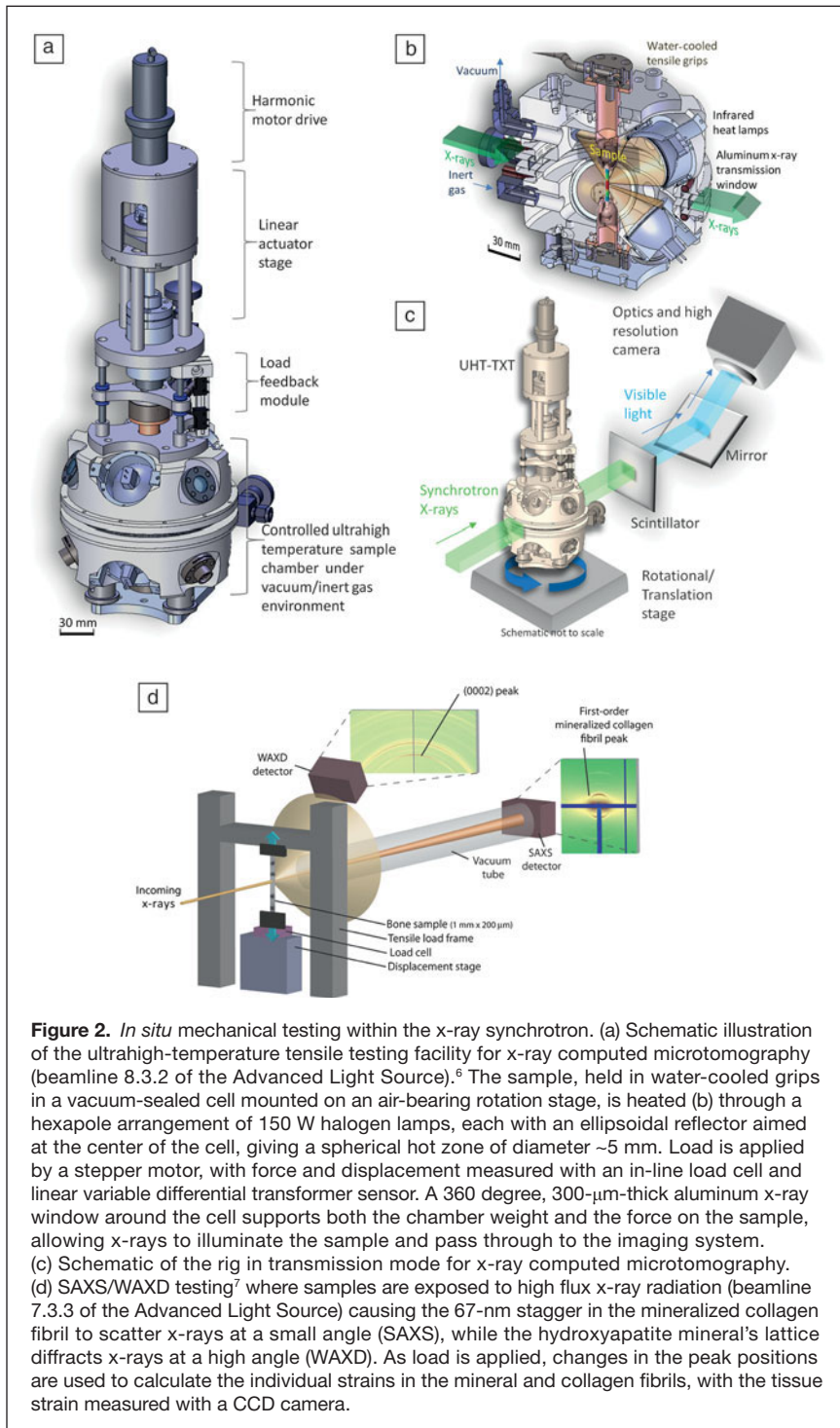


Figure 2. *In situ* mechanical testing within the x-ray synchrotron. (a) Schematic illustration of the ultrahigh-temperature tensile testing facility for x-ray computed microtomography (beamline 8.3.2 of the Advanced Light Source).⁶ The sample, held in water-cooled grips in a vacuum-sealed cell mounted on an air-bearing rotation stage, is heated (b) through a hexapole arrangement of 150 W halogen lamps, each with an ellipsoidal reflector aimed at the center of the cell, giving a spherical hot zone of diameter ~5 mm. Load is applied by a stepper motor, with force and displacement measured with an in-line load cell and linear variable differential transformer sensor. A 360 degree, 300- μm -thick aluminum x-ray window around the cell supports both the chamber weight and the force on the sample, allowing x-rays to illuminate the sample and pass through to the imaging system. (c) Schematic of the rig in transmission mode for x-ray computed microtomography. (d) SAXS/WAXD testing⁷ where samples are exposed to high flux x-ray radiation (beamline 7.3.3 of the Advanced Light Source) causing the 67-nm stagger in the mineralized collagen fibril to scatter x-rays at a small angle (SAXS), while the hydroxyapatite mineral's lattice diffracts x-rays at a high angle (WAXD). As load is applied, changes in the peak positions are used to calculate the individual strains in the mineral and collagen fibrils, with the tissue strain measured with a CCD camera.

using monochromatic and polychromatic x-rays. We employ a unique facility at the Advanced Light Source at the Lawrence Berkeley National Laboratory (LBNL) that permits *in situ* characterization at temperatures up to 1850°C in inert or oxidizing atmospheres with the capability to maintain a controlled tensile/compressive load on the sample, while simultaneously imaging in 3D in real time with 650 nm/voxel spatial resolution (Figure 2).⁶ For each scan, a set of 1200

radiographs are collected and converted to a reconstructed 3D tomographic image using inverse radon transforms. Images formed with the coherent x-ray source contain both phase and absorption contrast, which emphasizes edges and makes quantitative measurement of crack openings difficult. To minimize phase-contrast effects, we used the Modified Bronnikov Algorithm and filtered back-projection to obtain 3D tomographic reconstructions of the phase signal, enabling more accurate quantitative structural measurements.⁹

In situ eSEM fracture-toughness testing

A simple yet effective technique to characterize fracture-toughness behavior with real-time observation of how growing cracks interact with the salient microstructural features is to perform measurements within the eSEM. For bone, we load hydrated bone samples with a Gatan Microtest 2 kN three-point bending stage in the eSEM and monitor stable crack extension as a function of the “crack-driving force” to determine R-curves.^{10,11} We use nonlinear-elastic fracture mechanics with the crack-driving force defined using the J -integral,¹² as this includes the plasticity contribution to the toughness. Full details are given elsewhere.^{10,12}

Fracture resistance in bone

Human bone tissue can be either trabecular (spongy) or cortical (compact). Trabecular bone, also known as cancellous bone, fills the insides of many bones with struts on the order of 100–300 μm in diameter. In this work, we have focused on cortical bone, which is a nanocomposite of principally Type I collagen molecules[†] and hydroxyapatite mineral nanocrystals.¹ Its essential mechanical properties of stiffness (~15–25 GPa), strength (~100 MPa), and toughness (≥ 5 MPa/m) are derived at multiple length scales throughout bone's hierarchical architecture.

Bone's intrinsic toughness,² which arises from mechanisms that inhibit both the initiation and growth of cracks, can be identified

with plasticity (strictly inelasticity) mechanisms acting ahead of a crack and derived primarily at submicron length scales from collagen fibrillar sliding (Figure 1). Extrinsic

[†]There are several different types of collagen in the human body that can be distinguished by their chemical compositions. Type I is considered to be the most abundant and is found in bones and skin.

toughening mechanisms,^{2,3} conversely, act primarily in the crack wake to inhibit cracking by “shielding” the applied stresses; they are created in bone at micron scales principally by the interaction of growing cracks with the osteonal structures to induce crack deflection and form crack bridges.¹⁰

Aging-related deterioration in bone

Biological factors such as aging and disease can increase the fracture risk in bone. Although this is attributed to a loss in bone-mineral density (bone quantity),¹³ recent studies show that the structure and properties of bone specifically degrade with age, independent of bone-mass¹⁴ (bone quality). Indeed, age-related deterioration in toughness^{7,11,15} has been correlated with several nano/microstructural changes, including increased microcracking, osteonal dimensions,^{7,16} and collagen cross-link densities.^{7,17} In human bone, cross-links occur as enzymatic cross-links, both immature intrafibrillar and mature interfibrillar, and non-enzymatic advanced glycation end-products (AGEs), such as pentosidine, that form intra- and interfibrillar links along the collagen backbone.¹⁸ While the level of enzymatic cross-links stabilizes at ~10–15 years of age, AGEs can increase up to fivefold with age, which has been correlated to reduced fracture resistance.¹⁹ Similarly, excessive remodeling with age increases the osteonal density in human cortical bone; this governs the degree of microcracking and, in turn, affects the development of crack bridges, which provide a major source of micron-scale toughening.¹¹

We examined the strength and toughness of hydrated human cortical bone (fresh frozen humeri; the bone in the arm extending from the shoulder to the elbow) from young (34–41 years), middle-aged (61–69 years), and aged (85–99 years) groups.⁷ Although yield and peak strengths show only a 5–10% drop with aging (Figure 3a), corresponding fracture-toughness properties, presented as stress-intensity *K*-based R-curves^{7,11} (Figure 3b), reveal a twofold decrease in crack-initiation toughness (defined as the stress intensity at which the crack extension $\Delta a \rightarrow 0$) and a fourfold decrease in crack-growth toughness (defined as the initial slope of the R-curve).

Fracture surfaces in the longitudinal orientation are generally relatively smooth, with evidence of microcrack formation nominally parallel to, and ahead of, the growing crack. The intact regions between these microcracks and the main growing crack result in the formation of “uncracked-ligament” bridges,³ which provide a source of extrinsic toughening by carrying load that would otherwise be used to further crack growth. The crack bridges, however, are smaller and fewer in number in aged bone (Figure 3c–d), signifying a reduced contribution to the crack-growth toughness with age.^{7,11} Microtomography of these samples demonstrated a higher number of osteons in aged bone (Figure 3c–d); in fact, the aged sample had nearly three times the osteonal density (On. Dn. is the number of osteons per unit area), consistent with trends of increased bone turnover with age (Figure 3e).²⁰ The reduced spacing between osteons in older bone is consistent with smaller crack bridges and lower crack-growth toughness.

To examine the intrinsic behavior at submicron dimensions, *in situ* high-flux synchrotron x-ray scattering experiments on uniaxial tensile specimens were used to study the mechanical behavior of the individual constituents of bone. Results from such SAXS/WAXD experiments were obtained as strains in the mineralized collagen fibrils (Figure 3f) and mineral as a function of the macroscopic strain applied to the sample (i.e., tissue strain).⁷ For a given tissue strain, the strain in the collagen is more than 25% lower in aged bone than in young bone, implying that the fibrils become essentially stiffer with age due to changes in the collagen environment.[‡] This was examined by quantifying the collagen cross-linking due to non-enzymatic glycation. Consistent with the literature,¹⁷ our results show a higher level of AGEs in aged bone than in young bone (Figure 3g). The SAXS/WAXD observations clearly indicate that these increased levels of non-enzymatic cross-links with age stiffen the collagen fibrils, thereby affecting the plasticity of the bone.

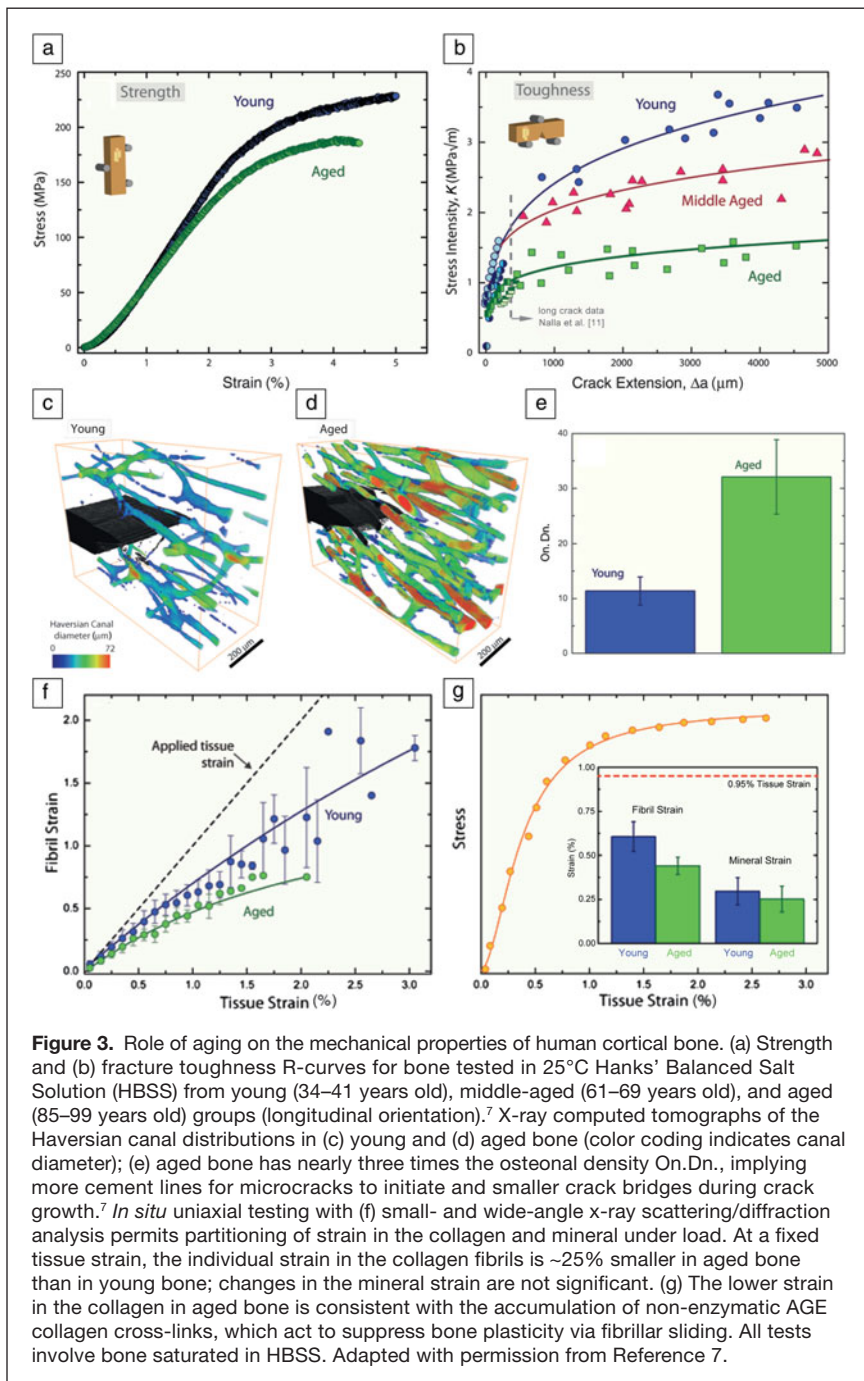
Disease-related deterioration in bone

In addition to aging, there are many diseases that can severely affect the mechanical properties of bone, making it more prone to fracture. We briefly describe one such example, that of *osteogenesis imperfecta* (OI), to show that although complex biological factors are involved, the specific reasons for the loss in bone strength can again be related to simple engineering principles, in particular to a consideration of the deterioration in intrinsic versus extrinsic toughening.²¹

OI, or “brittle bone” disease, is an affliction without a cure that affects some 1/15,000 births.²² It results from molecular mutations that lead to bone fragility and often spontaneous fractures and is characterized by low bone mass and strength and skeletal deformities from mutations of Type I collagen structure and quantity.^{23–25} OI patients have reduced cortical/trabecular bone volume, an increased presence of bone cells, both osteoblasts and osteoclasts with increased bone turnover, but lower mineral apposition rates not compensated by the increased cell number;^{24,25} they also show high mineral content and loss of mineralization heterogeneity,²⁵ all features that contribute to increased bone fragility.

We examined the effect of OI on bone fracture using a specific mouse model, the OI murine (*oim*) model,²¹ which is widely used in medical studies.²⁶ *Oim* mice naturally produce $\alpha 1(I)$ collagen homotrimers instead of normal heterotrimer $\alpha 1(I)2\alpha 1(I)$ collagen, a similar collagen mutation seen in human OI;²⁷ indeed, they exhibit phenotypic and biochemical features typical of human OI.²⁸ Specifically, homozygous *oim* mice (*oim/oim*) have spontaneous skeletal fractures, acute osteopenia (lower than normal bone mineral density), bone deformities with decreased body size; their cortical bone displays increased mineralization with

‡The mineral strain does not significantly change,⁷ principally because the hydroxyapatite has a stiffness roughly three orders of magnitude larger than the collagen.



decreased heterogeneity, with long bones and vertebrae showing little plastic deformation and reduced stiffness compared to healthy bone. Heterozygous *oim* mice (*oim*+) have the same collagen mutation with normal collagen.²⁹ Consequently, bones from *oim/oim* mimic severe human OI, whereas *oim*+ bones mimic mild OI with less severe osteopenia and no spontaneous fractures.²⁹

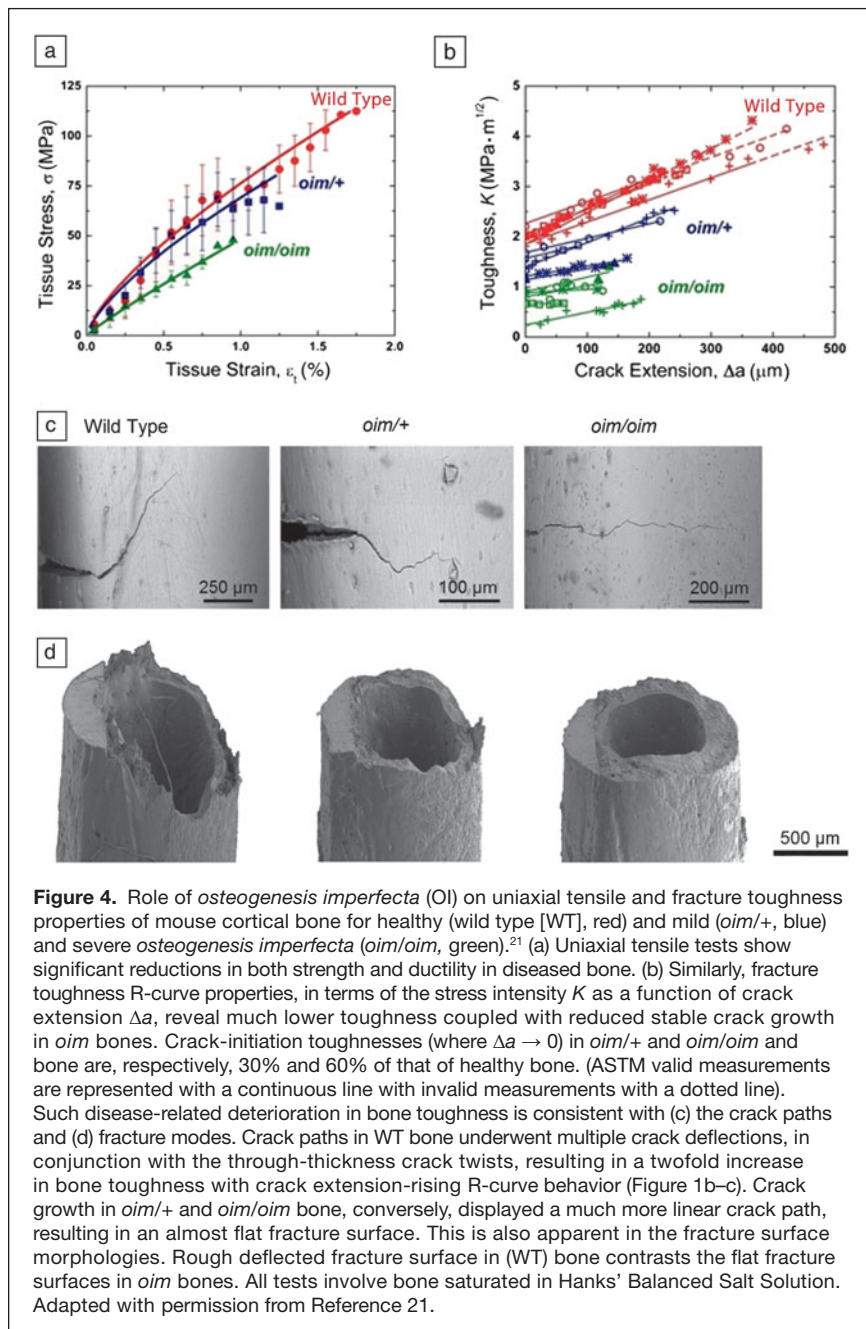
Uniaxial tensile testing of femora bone saturated in Hanks' Balanced Salt Solution (HBSS) was performed in the synchrotron to measure stress-strain curves. Results from *oim*+ and *oim/oim* bone are compared to normal, healthy (wild type, WT)

bone in **Figure 4a** and reveal a loss in stiffness, a 30–40% loss in ductility, and a 40–67% loss of strength in mild and severe OI bone, compared to healthy bone.²¹ *In situ* SAXS/WAXD analysis showed that at tissue strains >0.3%, the strain in the mineralized collagen fibrils was, respectively, 25% and 50% higher in *oim*+ and *oim/oim* bone than in normal bone, consistent with measurements showing changes in the collagen environment for both enzymatic and non-enzymatic AGE cross-links.²¹ The effects of OI at the scale of the collagen fibrils involve changes in the collagen cross-linking, which suppress plasticity by fibrillar sliding, thereby lowering strength and reducing ductility.

The extrinsic contribution originates at much higher length scales and is associated with the interactions of a growing crack with the bone-matrix structure. R-curves for the femora *oim*+ and *oim/oim* bone (transverse orientation) in **Figure 4b** reveal a 30–70% drop in toughness compared to healthy bone; moreover, the capacity for subcritical cracking is a factor of two lower in severe OI bone.²¹ Images of the fracture surfaces (**Figure 4c–d**) reveal that in diseased bone, cracks propagate with a smoother, non-tortuous path than in healthy bone, where growing cracks tend to deflect sharply, akin to crack deflection at the osteonal boundaries in human bone. Mouse bones do not have osteons or the Haversian canals (the tube-like structures that surround the blood vessels and nerve cells) inside them; their highest level of organization is in the concentric lamellae around their medullary cavity (the central cavity of the bone shaft that stores the marrow), but it is these interfaces between the bone's lamellar structure that can also result in deflection/twisting of the crack from the path of maximum tensile stress. As such deviations from the path of maximum "driving force" act to reduce the local stress intensity by roughly a factor of two (for a 90 degree deflection), this is a

particularly potent extrinsic toughening mechanism (it is why bone is more difficult to break in the transverse orientation than fracture by splitting in the longitudinal direction¹⁰). It is the absence of such deflected crack paths in OI bone that causes the loss in extrinsic toughness.

We believe that cracks deflect at the cement lines in healthy bone because these are regions of higher mineralization; indeed, it is this heterogeneity in the bone-matrix structure that is so critical to maintaining its resistance to fracture. In many forms of diseased bone, such as OI, abnormal mineralization leads not simply to a higher mineral content (which, in itself,



is embrittling) but to a greater homogeneity in mineralization²⁵ and structure; the relative mineralization between the cement line and the matrix is no longer so acute that the interface ceases to represent a “brittle” region to deflect cracks. We see similar effects in vitamin D deficient human bone,³⁰ which appears to be prematurely aged compared to healthy bone—again a greater homogeneity in mineralization results in less deflected crack paths. Indeed, this could be a contributing cause of atypical femoral fractures in bone subjected to bisphosphonate treatments³¹ where fracture surfaces tend to be uncharacteristically smooth.

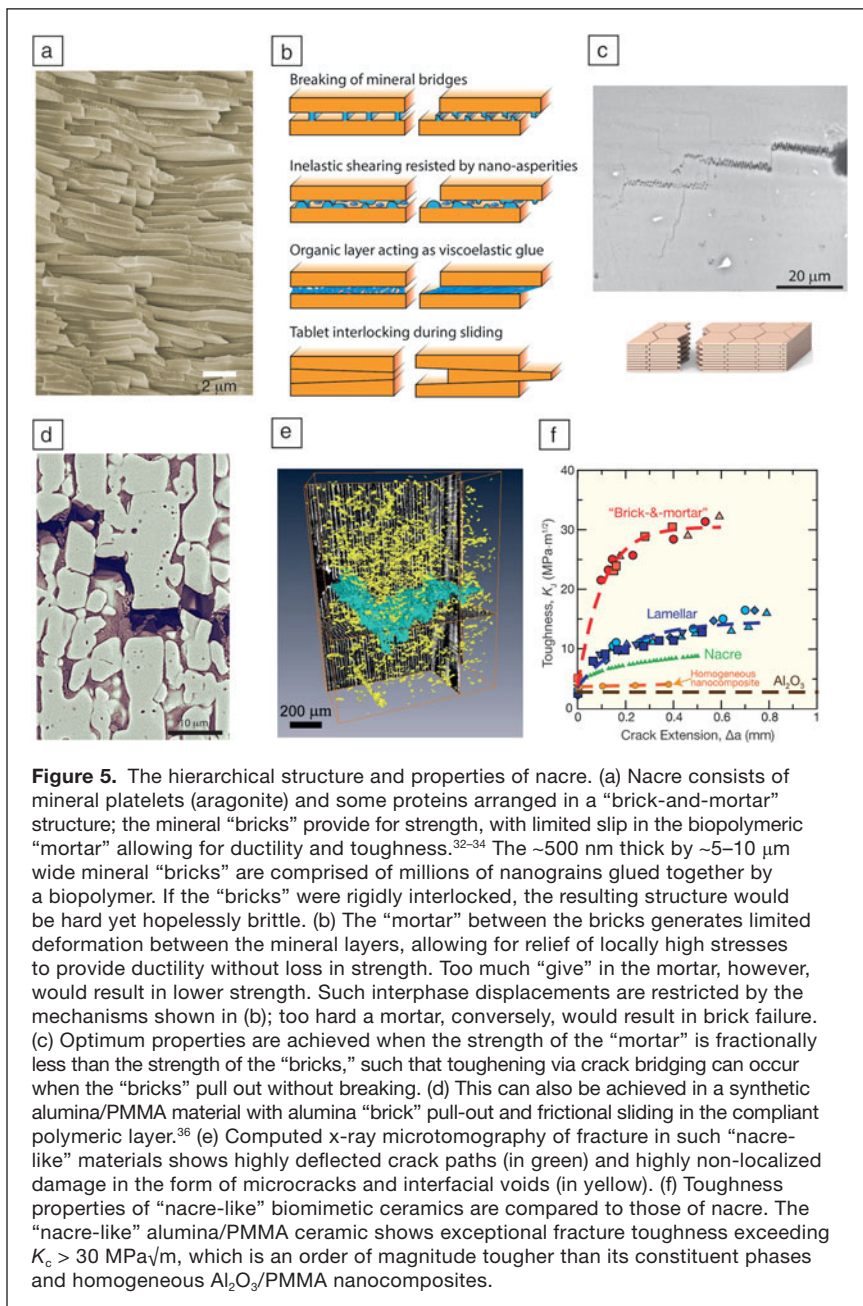
These intrinsic and extrinsic toughening mechanisms which originate at such widely differing length scales are coupled.⁷

Once cross-linking restricts plasticity by fibrillar sliding at molecular/fibril levels, the bone still must dissipate energy during deformation, which it does by microcracking at higher length scales. Not only does this provide the likely signaling process to instigate bone remodeling, but microcracking provides an essential precursor to the formation of the extrinsic crack bridging and deflection mechanisms.

In summary, the evidence at submicron length scales, from SAXS/WAXD analysis of uniaxial tensile tests, strongly suggests that intrinsic contributions to the bone's fracture resistance arise from its ability to plastically deform; aging and certain bone diseases result in changes to the collagen cross-linking environment, which specifically act to constrain this capacity in the form of restricted fibrillar sliding. The resulting loss in ductility at such nanometer length scales directly degrades the intrinsic toughness, thereby contributing to increased fracture risk. At coarser length scales in the micron to near-millimeter regime, evidence from eSEM and μ -CT fracture testing suggests a very different picture. The primary driver for extrinsic toughening is the crack path and its interaction with the bone-matrix structure, with the salient shielding mechanisms identified as crack bridging and deflection. Increased osteonal density, seen for example in aged bone, acts to diminish crack-bridging phenomena, which is a primary factor associated with the aging-related degradation in longitudinal bone toughness. An increase in the homogeneity in mineralization, seen for certain bone disease states, similarly acts to diminish crack-path tortuosity; the resulting loss in extrinsic toughening by crack deflection may be a primary factor in the increased fragility of diseased bone.

Bioinspired materials

Like bone, mollusk shells are another fine example of Nature's design of damage-tolerant materials. Dating back as a species to some 545 million years, these materials, such as nacre (red Abalone shell), have a “brick-and-mortar” structure; the “bricks,” comprising ~95 vol% of the structure, are ~0.5 μ m thick, 5–10 μ m wide platelets of the mineral aragonite (polymorph of calcium carbonate) separated by an organic biopolymer “mortar” (Figure 5).³² The mineral accounts for the high strength; however, as it is inherently brittle, if the aragonite platelets were rigidly locked together, the resulting toughness would be minimal, as there would



be no means to relieve locally high stresses. This is the role of the organic “mortar,” a compliant interphase that allows some movement between the platelets, thereby conferring intrinsic toughening.⁴ This sliding between the mineral platelets must be limited (~1 μm) though, or strength would be lost. Nature achieves this via the frictional resistance of the “mortar,” “frictional stops” from the surface roughness of the platelets, and from small mineral “bridges” linking the layers (Figure 5b).^{32–34} The tortuous crack paths and “pull-out” of the mineral platelets further provides extrinsic toughening (Figure 5c).³⁵ The result is a hybrid material with a toughness at least an order of magnitude higher than its constituent phases.

We have made bioinspired bulk ceramic materials in the image of the nacre structure (Figure 5d–f).³⁶ Using alumina powders mixed with water and frozen using a freeze-casting technique,³⁷ ceramic scaffolds are processed with layer thicknesses (~1–100 μm) controlled by the cooling rate and interlayer roughnesses controlled, in part, by a dopant addition (sugar, salt, alcohol). After cold pressing and infiltrating with a polymeric “compliant phase” (PMMA), “brick-and-mortar” 85 vol% alumina/PMMA (nacre-like) materials have been fabricated in bulk form. The resulting mechanical properties of these bioinspired ceramics are remarkable, with strengths comparable with pure alumina but toughesses an order of magnitude larger. Indeed, fracture toughesses can exceed 30 MPa \sqrt{m} (Figure 5f), making these materials the toughest ceramics on record.³⁶ Toughening is achieved primarily through ceramic brick pull-out, with optimal damage-tolerance achieved with a resistant “mortar” displaying a strength just below the brick strength (so that the bricks do not fracture) (Figure 5d). *In situ* computed tomography clearly reveals additional toughening from marked crack deflection, and from the fact that local damage from interfacial voids and microcracks is widely dispersed and not prone to localization (Figure 5e).

Ceramic-matrix composites

At the other extreme of material behavior, we consider structural materials designed for ultrahigh-temperature applications such as gas turbines.³⁸ Over the past ~80 years, the development of gas turbines for propulsion and power generation, from Frank Whittle’s first models in the 1930s–1940s to commercial and military aircraft engines used today, can be linked to the use of superior elevated-temperature materials.

This has enabled progressively higher operational temperatures (with blade temperatures rising from 800°C in the 1940s to 1100°C or more today) with consequent major fuel savings and increases in thermodynamic efficiency—this is the turbine equivalent of Moore’s Law for computer-chip speeds! Currently, turbine blades made from single-crystal nickel-based superalloys can function at temperatures ~1150°C.³⁹ However, this represents a thermodynamic upper-limit, which can be extended by thermal-barrier coatings and forced-air cooling, although this greatly reduces the efficiency gained from higher-temperature operation. Ceramic components, conversely, have the potential for uncooled operation at temperatures several hundred degrees hotter with markedly reduced structural weight, but their use

has been compromised by uncertain damage-tolerance. The development of ceramic-matrix composites, in particular silicon carbide matrix ceramics reinforced with silicon carbide fibers ($\text{SiC}_f\text{-SiC}_m$), may change this;^{40–42} indeed, CMCs are slated for use in commercial aircraft engines by the end of this decade.

In addition to gas turbines, CMCs are candidate materials for control surfaces in potential hypersonic vehicles requiring further extremes of temperatures (1500°C or more).⁴³ For these applications, textile composites with 3D-woven carbon or SiC fibers embedded within a chemical-vapor-infiltrated (CVI) SiC matrix demonstrate the best thermal and mechanical properties.^{40–43} Weak fiber-matrix interfaces, engineered using boron nitride or pyrolytic-carbon coatings, enable fiber-bridging mechanisms for damage-tolerance; the resulting difference in strain between matrix and fiber failure imparts a degree of “ductility” that is absent in monolithic ceramics.⁴⁴ Owing to their complicated architectures, failure mechanisms are invariably complex, occurring at several length scales as matrix cracking, individual fiber breaks, fiber bundle (or tow) fractures, splitting cracks between individual fibers within tows, and delaminations between fiber tows. For CMCs to reach sufficient maturity to be used as structural materials at such extreme temperatures, a thorough quantitative understanding of their damage/failure mechanisms under load in realistic service environments must be achieved.^{44,45} This is particularly critical for design and life prediction.

Measurements at temperature are the only faithful means to characterize such damage and failure processes. Cooling to ambient temperatures for examination introduces thermal strains, ~0.1–0.5%, depending on composition and cooling rate, which can change cracking patterns. *In situ* x-ray tomographic observations represent a means to gain such detailed quantitative mechanistic information under load at temperature in 3D.³⁸

Using our μ -CT facility for 3D imaging (Figure 2),^{6,38} we examined damage mechanisms in $\text{SiC}_f\text{-SiC}_m$ under *in situ* tensile loading at 1750°C. Single tow specimens of BN-coated SiC fibers (Nippon Carbon Hi-Nicalon Type-S, 500 fibers/tow, fiber diameter 10 μm) embedded within a CVI SiC matrix, were bonded into threaded molybdenum grips and mounted in a self-aligning ball-and-socket loading fixture. Tomography data were collected by imaging $\text{SiC}_f\text{-SiC}_m$ specimens over a 5 mm gauge length at room temperature and 1750°C, while tensile forces were applied in steps by a displacement-controlled loading system; details are given elsewhere.³⁸

Individual fibers and BN coatings were readily resolved in cross-sectional slices normal to fiber tows (Figure 6) with no discernible

difference in resolution (650 nm/voxel) at all temperatures. Matrix cracks developed during loading at low temperatures and extended continuously, with the entire load carried by intact fibers bridging these cracks. Most matrix cracks comprised a single planar surface normal to the applied load, although some followed a helical path around the fiber axis. At low temperatures, multiple cracks were formed; at high temperatures, failure was associated with a single dominant crack that branched before instability. Just below peak load, broken fibers were detected throughout the composite; the number increased at higher loads before the fibers were pulled-out from the matrix. The 3D images reveal a wealth of information on the events occurring in the interior of the composite during failure (Figure 7): loads and locations where individual fibers fractured, distances the fibers relaxed after breaking, opening displacements of the matrix cracks, and 3D surfaces of the matrix cracks.

Crack bridging is essential to toughening these materials;⁴⁴ it is enabled by the weak BN interphase, allowing debonding and fiber/matrix sliding. The magnitude of sliding resistance dictates how multiple cracks form in the matrix,⁴⁵ which dictates the composite’s macroscopic stress-strain

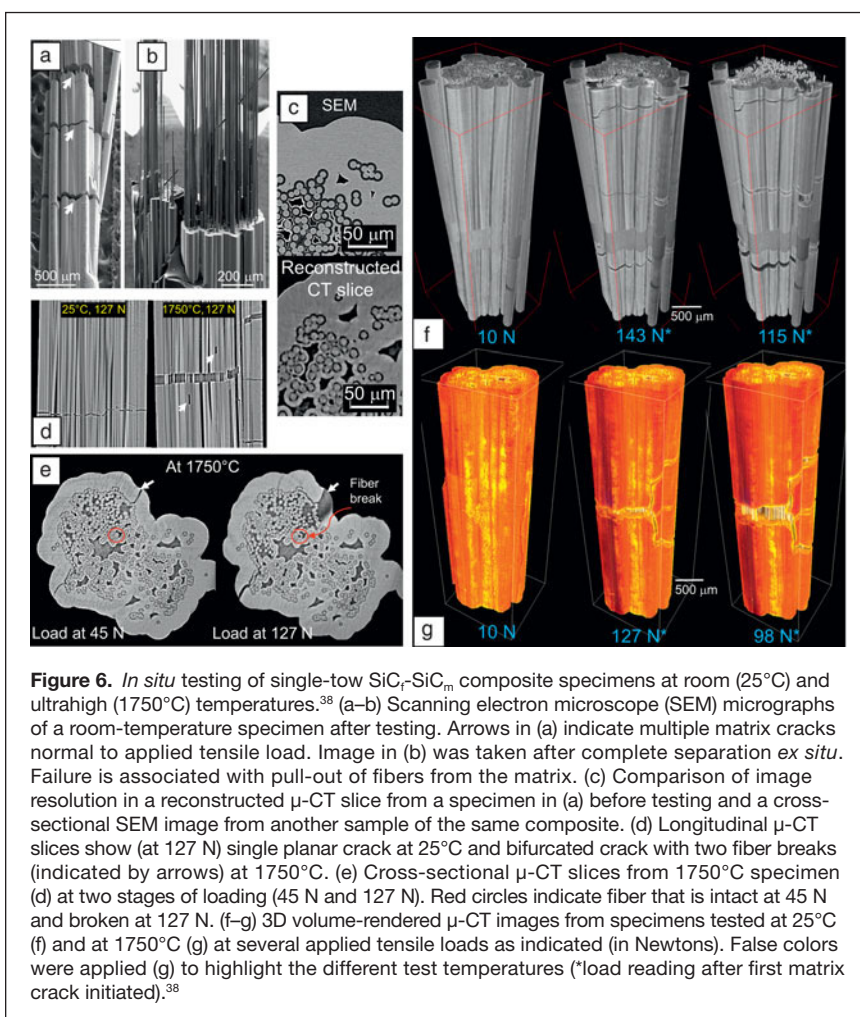
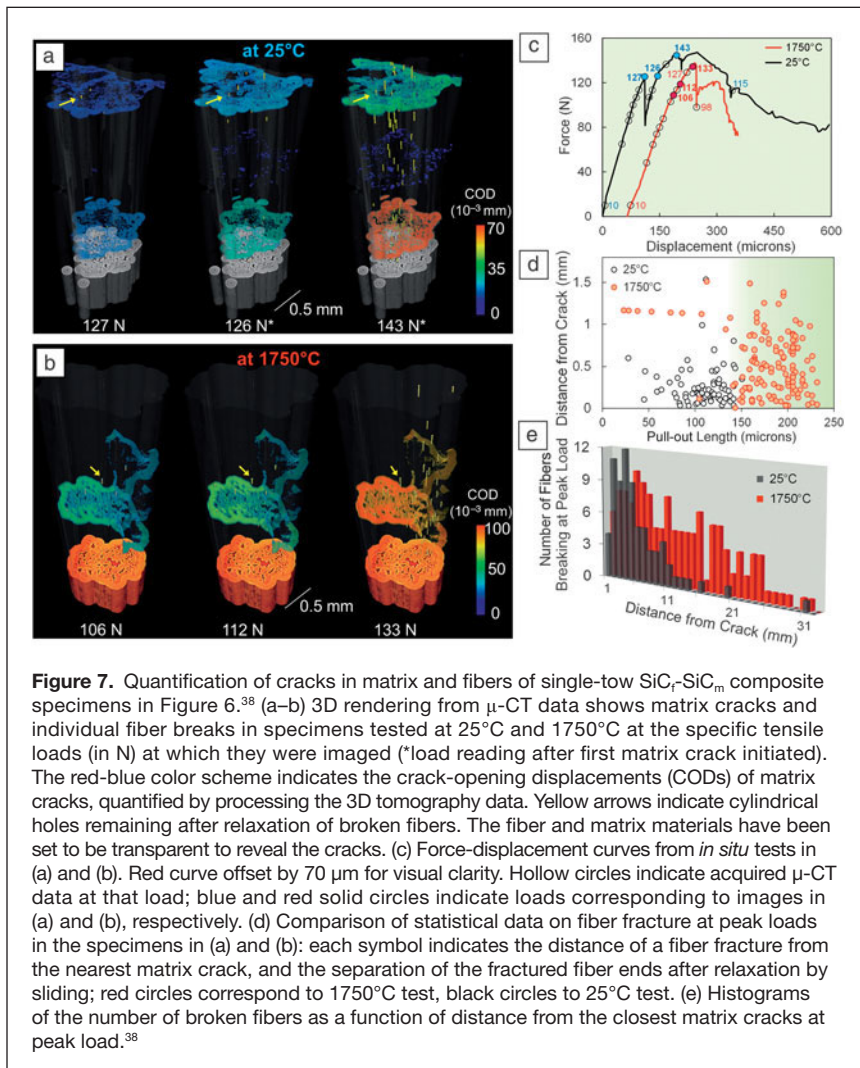


Figure 6. *In situ* testing of single-tow $\text{SiC}_f\text{-SiC}_m$ composite specimens at room (25°C) and ultrahigh (1750°C) temperatures.³⁸ (a–b) Scanning electron microscope (SEM) micrographs of a room-temperature specimen after testing. Arrows in (a) indicate multiple matrix cracks normal to applied tensile load. Image in (b) was taken after complete separation *ex situ*. Failure is associated with pull-out of fibers from the matrix. (c) Comparison of image resolution in a reconstructed μ -CT slice from a specimen in (a) before testing and a cross-sectional SEM image from another sample of the same composite. (d) Longitudinal μ -CT slices show (at 127 N) single planar crack at 25°C and bifurcated crack with two fiber breaks (indicated by arrows) at 1750°C. (e) Cross-sectional μ -CT slices from 1750°C specimen (d) at two stages of loading (45 N and 127 N). Red circles indicate fiber that is intact at 45 N and broken at 127 N. (f–g) 3D volume-rendered μ -CT images from specimens tested at 25°C (f) and at 1750°C (g) at several applied tensile loads as indicated (in Newtons). False colors were applied (g) to highlight the different test temperatures (*load reading after first matrix crack initiated).³⁸



response. Specifically, the friction stress determines a limiting lower-bound for the applied tensile stress, at which matrix cracking can occur,⁴⁶ as well as a characteristic length over which sliding occurs and stress is transferred between the fibers and matrix. The sliding distance determines the spacing and opening displacements of matrix cracks and the relaxation of fibers that are broken within the matrix; this is responsible for the nonlinear stress-strain response after the onset of inelastic behavior.

Indeed, the tomography images reveal changes in the sliding resistance at 1750°C. First, at a given load, the matrix crack-opening displacement was larger at 1750°C (Figure 7). Provided the sliding zones of adjacent cracks do not overlap and a significant number of fibers remain unbroken, the frictional stress can be calculated from the crack-opening displacements. Using the images at 127 N load in Figures 6 and 7, frictional stresses of 2 MPa at 25°C and 0.4 MPa at 1750°C, respectively, were estimated, giving sliding lengths (and thus crack spacings) of ~ 3 mm at 25°C and ~ 13 mm at 1750°C. Second, multiple matrix cracks formed within the test

section at 25°C, at loads between the imaging steps at 113 and 127 N, whereas at 1750°C, a single crack formed at 45 N load (Figure 6). In both cases, the crack-opening displacements continued to increase with further loading, with no new cracks formed.

The room-temperature results and calculated sliding lengths are consistent with observations from separate *ex situ* tests on larger samples that showed a distribution of cracks separated by distances of 1 to 4 mm. At high temperatures, observations of a single crack are also consistent with calculated sliding lengths exceeding half the gauge length. Third, differences were seen in the statistical distributions of fiber failure sites and relaxation lengths at both temperatures (Figure 7). The distributed loads and positions of fiber fractures relate directly to the statistical distribution of fiber strengths⁴⁷ and can be used to evaluate the parameters characterizing this distribution. At high temperature, failure sites were distributed over larger distances from the matrix cracks, and the relaxation distances were larger than at 25°C. These observations are also consistent with the sliding resistance being smaller at 1750°C than at 25°C, possibly associated with changes in residual stresses due to thermal-expansion mismatch.

Clearly *in situ* tomography can provide crucial information on the *in situ* behavior of CMCs under load in extreme temperature environments. We believe that there is currently no other way to access this information. Such data can reveal details about damage evolution that would otherwise remain invisible;

the standard methods based on sectioning at room temperature after high-temperature testing are unreliable because damage states likely will change due to thermal strains on cooling. Indeed, the acquisition of high-resolution images at such high temperatures may well transform the way in which design and qualification are carried out for these complex materials. The qualitative observations of damage emerging from the 3D *in situ* imaging inform us of what mechanisms must be represented in high-fidelity simulations, while quantitative measurements of, for example, the displacement vectors of internal cracks serve to calibrate the nonlinear fracture cohesive laws that govern crack evolution in simulations, all information vital for comprehensive design and life-prediction strategies.⁴⁵

Summary

This article has highlighted some of the advantages of using real-time imaging of mechanical behavior at multiple length scales to discern the origins of damage-tolerance in biological, biomimetic, and structural materials, specifically

bone, “nacre-like” ceramics and ceramic-matrix composites. From the perspective of understanding the sources of strength and toughness, *in situ* SAXS/WAXD techniques can provide quantitative information on the nature of the plasticity mechanisms that contribute to intrinsic toughening, whereas *in situ* eSEM and computed x-ray tomography of how a growing crack interacts with salient microstructural features can provide similar information on crack-tip shielding mechanisms, primarily crack deflection and bridging, that serve to induce extrinsic toughening. By applying these techniques to the study of the fragility of bone, we have shown how bone generates its damage-tolerance at differing length scales and how this can degrade due to biological factors such as aging and disease.

With respect to next-generation high-temperature structural materials, such as the CMCs described here, the use of real-time x-ray microtomography for samples under load represents a vital technique for characterizing damage at temperature. The tomography data contain complete quantitative information on crack paths, crack-surface areas and orientations, spatial variations in the crack-opening displacements, statistics of relative spatial location of cracks, and microstructural heterogeneities within the sample volume—all parameters that are critical in any analysis of fracture. The challenge is to extract this information from reconstructed 3D images in a form that can be used for validation of computational models and to provide calibration of material constitutive laws as input for the models. Success rests on efficient methods for processing the 3D image data with techniques such as segmentation for automated identification and representation of cracks and microstructural features.

Acknowledgments

I thank my colleagues, postdocs, and students who participated in this work, especially Drs. Tony Tomsia, Bernd Gludovatz, Hrishi Bale, Max Launey, Alessandra Carriero, and Liz Zimmermann. Thanks also to Dr. Simon Tang for his cross-linking measurements, Drs. David Marshall and Brian Cox

for their involvement in our CMC research, and the Lawrence Berkeley National Laboratory’s Advanced Light Source (ALS) beamline scientists Dr. Alastair MacDowell and Eric Schaible for help with our synchrotron studies. Work on mechanical properties/biomimetic materials was funded by the Department of Energy, Office of Basic Energy Sciences, Materials Sciences and Engineering Division, under contract DE-AC02-05CH11231, which also supports the x-ray synchrotron beamlines 7.3.3 (SAXS/WAXD) and 8.3.2 (microtomography) at the ALS. Studies on bone were supported by the National Institute of Health (NIH/NIDCR) under grant 5R01 DE015633, and on CMCs by AFOSR/NASA via Teledyne under contract FA9550-09-1-0477.

To view a video of Robert O. Ritchie’s presentation at the MRS 2013 Fall Meeting, visit www.mrs.org/2013-mrs-fall-meeting-on-demand/.

References

1. S. Weiner, H.D. Wagner, *Annu. Rev. Mater. Res.* **28**, 271 (1998).
2. M.E. Launey, M.J. Buehler, R.O. Ritchie, *Annu. Rev. Mater. Res.* **40**, 25 (2010).
3. R.K. Nalla, J.H. Kinney, R.O. Ritchie, *Nat. Mater.* **2**, 164 (2003).
4. R.O. Ritchie, *Nat. Mater.* **10**, 817 (2011).
5. H.S. Gupta, J. Seto, W. Wagermeier, P. Zaslansky, P. Boesecke, P. Fratzl, *Proc. Natl. Acad. Sci. U.S.A.* **103**, 17741 (2006).
6. A. Haboub, H.A. Bale, J.R. Nasiatka, B.N. Cox, D.B. Marshall, R.O. Ritchie, A.A. MacDowell, *Rev. Sci. Instrum.* **85**, 83702 (2014).
7. E.A. Zimmermann, E. Schaible, H. Bale, H.D. Barth, S.Y. Tang, P. Reichert, B. Busse, T. Alliston, J.W. Ager, R.O. Ritchie, *Proc. Natl. Acad. Sci. U.S.A.* **108**, 14416 (2011).
8. H.D. Barth, E.A. Zimmermann, E. Schaible, S.Y. Tang, T. Alliston, R.O. Ritchie, *Biomaterials* **32**, 8892 (2011).
9. A. Groso, R. Abela, M. Stambanoni, *Opt. Express* **14**, 8103 (2006).
10. K.J. Koester, J.W. Ager, R.O. Ritchie, *Nat. Mater.* **7**, 672 (2008).
11. R.K. Nalla, J.J. Kruzic, J.H. Kinney, M. Balooch, J.W. Ager, R.O. Ritchie, *Mater. Sci. Eng. C* **26**, 1251 (2006).
12. T.L. Anderson, *Fracture Mechanics: Fundamentals and Applications* (CRC Press, Boca Raton, FL, 2005).
13. S.R. Cummings, W. Browner, D.R. Black, M.C. Nevitt, H.K. Genant, J. Cauley, K. Ensrud, J. Scott, T.M. Vogt, *Lancet* **341**, 72 (1993).
14. S.L. Hui, C.W. Slemenda, C.C. Johnston, *J. Clin. Invest.* **81**, 1804 (1988).
15. P. Zioupos, J.D. Currey, *Bone* **22**, 57 (1998).
16. R.W. McCalden, J.A. McGeough, M.B. Barker, C.M. Courtbrown, *J. Bone Joint Surg. Am.* **75A**, 1193 (1993).
17. D.R. Sell, V.M. Monnier, *J. Biol. Chem.* **264**, 21597 (1989).
18. A.J. Bailey, *Mech. Ageing Dev.* **122**, 735 (2001).



2014 MRS®
FALL MEETING & EXHIBIT
November 30 - December 5, 2014 | Boston, Massachusetts

REGISTER BY NOVEMBER 14
▶ AND SAVE!

Reserve Your Exhibit Space Now www.mrs.org/fall2014

19. D. Vashishth, G.J. Gibson, J.I. Khoury, M.B. Schaffler, J. Kimura, D.P. Fyhrie, *Bone* **28**, 195 (2001).
 20. B. Busse, M. Hahn, T. Schinke, K. Püschel, G.N. Duda, M. Amling, *J. Biomed. Mater. Res. A* **92A**, 1440 (2010).
 21. A. Carriero, E.A. Zimmermann, A. Paluszny, S.Y. Tang, H. Bale, B. Busse, T. Alliston, G. Kazakia, R.O. Ritchie, S.J. Shefelbine, *J. Bone Miner. Res.* **29**, 1392 (2014).
 22. A. Forlino, W.A. Cabral, A.M. Barnes, J.C. Marini, *Nat. Rev. Endocrinol.* **7**, 540 (2011).
 23. W.G. Cole, *Clin. Orthop. Relat. Res.* **401**, 6 (2002).
 24. F. Rauch, F.H. Glorieux, *Lancet* **363**, 1377 (2004).
 25. W. Traub, T. Arad, U. Vetter, S. Weiner, *Matrix Biol.* **14**, 337 (1994).
 26. R. Bargman, A. Huang, A.L. Boskey, C. Raggio, N. Pleshko, *Connect. Tissue Res.* **51**, 123 (2010).
 27. A.C. Nicholls, G. Osse, H.G. Schloon, H.G. Lenard, S. Deak, J.C. Myers, D.J. Prockop, W.R.F. Weigel, P. Fyrer, F.M. Pope, *J. Med. Genet.* **21**, 257 (1984).
 28. M. Vanleene, S.J. Shefelbine, *Bone* **53**, 507 (2013).
 29. J. Saban, M.A. Zussman, R. Havey, A.G. Patwardhan, G.B. Schneider, D. King, *Bone* **19**, 575 (1996).
 30. B. Busse, H.A. Bale, E.A. Zimmermann, B. Panganiban, H.D. Barth, A. Carriero, E. Vettorazzi, J. Zustin, M. Hahn, J.W. Ager, K. Püschel, M. Amling, R.O. Ritchie, *Sci. Transl. Med.* **5**, 193ra88 (2013).
 31. B. Ettinger, D.B. Burr, R.O. Ritchie, *Bone* **55**, 495 (2013).
 32. M.A. Meyers, P.Y. Chen, A.Y.M. Lin, Y. Seki, *Prog. Mater. Sci.* **53**, 1 (2008).
 33. F. Barthelat, H. Tang, P.D. Zavattieri, C.M. Li, H.D. Espinosa, *J. Mech. Phys. Solids* **55**, 306 (2007).
 34. R.Z. Wang, Z. Suo, A.G. Evans, N. Yao, I.A. Aksay, *J. Mater. Res.* **16**, 2485 (2001).
 35. Y. Shao, H.-P. Zhao, X.-Q. Feng, H. Gao, *J. Mech. Phys. Solids* **60**, 1400 (2012).
 36. E. Munch, M.E. Launey, D.H. Alsem, E. Saiz, A.P. Tomsia, R.O. Ritchie, *Science* **322**, 1516 (2008).
 37. S. Deville, E. Saiz, R.K. Nalla, A.P. Tomsia, *Science* **311**, 515 (2006).
 38. H.A. Bale, A. Haboub, A.A. MacDowell, J.R. Nasiatka, D.L. Parkinson, B.N. Cox, D.B. Marshall, R.O. Ritchie, *Nat. Mater.* **12**, 40 (2013).
 39. D.M. Dimiduk, J.H. Perepezko, *MRS Bull.* **28**, 639 (2003).
 40. D.B. Marshall, B.N. Cox, *Annu. Rev. Mater. Res.* **38**, 425 (2008).

41. G.N. Morscher, H.M. Yun, J.A. DiCarlo, *J. Am. Ceram. Soc.* **88**, 146 (2005).
 42. K. Nakano, A. Kamiya, Y. Nishino, T. Imura, T.W. Chou, *J. Am. Ceram. Soc.* **78**, 2811 (1995).
 43. S. Schmidt, S. Beyer, H. Immich, H. Knabe, R. Meistring, A. Gessler, *Int. J. Appl. Ceram. Technol.* **2**, 85 (2005).
 44. D.B. Marshall, A.G. Evans, *J. Am. Ceram. Soc.* **68**, 225 (1985).
 45. B.N. Cox, H.A. Bale, M. Begley, M. Blacklock, B.-C. Do, T. Fast, M. Naderi, M. Novak, V.P. Rajan, R.G. Rinaldi, R.O. Ritchie, M.N. Rossol, J.H. Shaw, O. Sudre, Q.D. Yang, F.W. Zok, D.B. Marshall, *Annu. Rev. Mater. Res.* **44**, 479 (2014).
 46. B. Budiansky, A.G. Evans, J.W. Hutchinson, *Int. J. Solids Struct.* **32**, 315 (1995).
 47. T. Okabe, M. Nishikawa, W.A. Curtin, *Compos. Sci. Technol.* **68**, 3067 (2008). □



Robert O. Ritchie is the Chua Distinguished Professor in the Materials Science and Engineering Department at the University of California, Berkeley, and Faculty Senior Scientist at the Lawrence Berkeley National Laboratory. He has MA, PhD, and ScD degrees in physics/materials science from Cambridge University. Before joining Berkeley in 1981, he was an Associate Professor of Mechanical Engineering at the Massachusetts Institute of Technology. He is known for his research on the fracture of structural and biological materials, having authored over 650 papers. His current interests focus on the biological deterioration of bone, fracture in ultrahigh-temperature composites, and bioinspired structural materials. He is a member of the National Academy of Engineering, the UK Royal Academy of Engineering, the Russian Academy of Sciences, and the Swedish Academy of Engineering Sciences. Ritchie can be reached at the Department of Materials Science and Engineering, University of California, Berkeley, USA; tel. 510-486-5798; and email roritche@lbl.gov.

MRS OnDemand®

Experience the collaborative, interdisciplinary Materials Research Society community online, at your convenience.

Watch **Robert O. Ritchie**, University of California, Berkeley, present the 2013 MRS Fall Meeting David Turnbull Lecture FREE via MRS OnDemand.

Real-Time Imaging of the Structure and Mechanical Properties of Engineering and Biological Materials at Multiple Length-Scales

www.mrs.org/f13-turnbull-video



Your MRS, Your Way!
www.mrs.org/ondemand